PROCESSING OF MEASURED FIELDS USING ADVANCED INVERSE METHOD OF MOMENTS ALGORITHM

E. Jørgensen[1], **P. Meincke**[1], **O. Borries**[1], **and M. Sabbadini**[2]

[1]*TICRA, Læderstræde 34, DK-1201 København K, Denmark, ej@ticra.com, pme@ticra.com, ob@ticra.com*
[2]*ESA/ESTEC, 2200 AG Noordwijk, The Netherlands, Marco.Sabbadini@esa.int*

ABSTRACT

A higher-order inverse method of moments algorithm, employing smooth current and geometry representations, as well as a very noise-robust solution algorithm, was presented at last year's ESA workshop. The fundamental properties of the algorithm, including quantitative results for the RMS error of the reconstructed surface currents, were illustrated using synthetic data with added noise. In this paper we investigate the properties of an iterative variant of the algorithm and show practical results from applying the higher-order algorithm to measured fields obtained in a spherical near field range. The presented examples are chosen to illustrate both antenna diagnostics and filtering applications.

Key words: Higher-order method of moments, antenna diagnostics, filtering, source reconstruction.

1. INTRODUCTION

The inverse method of moments (INV-MoM) has been investigated by several research groups as a promising technique for reconstruction of extreme near fields and surface currents on arbitrary 3D surface surfaces enclosing the antenna from measured fields [1]-[14]. The application areas of INV-MoM include classical antenna diagnostics – where electrical or mechanical errors can be identified by inspection of the reconstructed near field or surface current– as well as filtering – where, for instance, currents on parts of the enclosing surface are artificially removed or radiation patterns of noisy, truncated, or irregular measurements are enhanced.

A higher-order version of the INV-MoM employing smooth current and geometry representations, as well as a very noise-robust solution algorithm based on Tiknonov regularization in generalized form, was presented at last year's ESA workshop [14]. In this paper we present an iterative variant of our regularization algorithm and subsequently apply the higher-order INV-MoM to measured fields obtained in the DTU-ESA spherical near-field test facility [15]. The first example illustrates the antenna diagnostics application and involves processing of the radiation pattern of a radiating element on a large satellite. It is shown that even small errors with only minor effect on the radiation pattern, e.g., a few dBs 30 dB below the peak level, can be clearly detected in the reconstructed surface currents. The second example, illustrating the filtering capabilities, deals with measurements performed on a corrugated horn antenna. A comparison with an analytical horn model shows that the INV-MoM can be used to reconstruct a noise-free radiation pattern recovering fine pattern details that were lost due to noise. Hence, in this application the INV-MoM acts as a physics-based filter providing enhanced measurement accuracy.

2. SUMMARY OF HIGHER-ORDER INVERSE METHOD OF MOMENTS

The higher-order INV-MoM is aimed at computing tangential electric and magnetic fields on the reconstruction surface S enclosing an antenna, based on fields measured at discrete points outside the surface. On the reconstruction surface, the equivalent electric and magnetic surface current densities are defined as

$$\mathbf{J}_S = \hat{\mathbf{n}} \times \mathbf{H} \tag{1a}$$

$$\mathbf{M}_S = -\hat{\mathbf{n}} \times \mathbf{E}, \tag{1b}$$

where $\mathbf{E}$ and $\mathbf{H}$ are the fields just outside the surface of reconstruction. These equivalent currents are those corresponding to Love's equivalence principle since they produce zero field inside S. They also correspond to the tangential physical fields one would actually measure on S.

The measured field can now be written as

$$\mathbf{E}^{\text{meas}}(\mathbf{r}) = -\eta_0 \mathcal{L}\mathbf{J}_S + \mathcal{K}\mathbf{M}_S \tag{2}$$

where η_0 is the free-space impedance and the integral operators $\mathcal{L}$ and $\mathcal{K}$ are defined as

$$\mathcal{L}\mathbf{J}_S = j\omega\mu_0 \Bigg[\int_S \mathbf{J}_S(\mathbf{r}') G(\mathbf{r}, \mathbf{r}')\, dS' + \frac{1}{k_0^2} \int_S \nabla'_S \cdot \mathbf{J}_S(\mathbf{r}') \nabla G(\mathbf{r}, \mathbf{r}')\, dS' \Bigg], \tag{3a}$$

$$\mathcal{K}\mathbf{M}_S = \int_S \mathbf{M}_S(\mathbf{r}') \times \nabla G(\mathbf{r}, \mathbf{r}')\, dS', \tag{3b}$$

where k_0 is the free-space wavenumber and $G(\mathbf{r}, \mathbf{r}')$ is the scalar Green's function of free space. Equation (2) is referred to as the data equation, since it relates the measured data $\mathbf{E}^{meas}$ and the unknown surface current densities $\mathbf{J}_S$ and $\mathbf{M}_S$.

Love's equivalent currents in (1) constitute just one set of possible equivalent currents that radiate exactly the field $\mathbf{E}^{\text{meas}}$ outside the reconstruction surface. Due to this ambiguity the desired physical current densities in (1) can only be obtained if additional a priori information is imposed. The desired currents in (1) are obtained by enforcing the a priori information that the fields radiated by ($\mathbf{J}_S$,$\mathbf{M}_S$) inside S must be zero [2], [13]. This leads to the equations

$$-\eta_0 \hat{\mathbf{n}} \times \mathcal{L}\mathbf{J}_S + \left(\hat{\mathbf{n}} \times \mathcal{K} + \frac{1}{2}\right)\mathbf{M}_S = 0, \qquad \text{(4a)}$$

$$-\left(\hat{\mathbf{n}} \times \mathcal{K} + \frac{1}{2}\right)\mathbf{J}_S - \frac{1}{\eta_0}\hat{\mathbf{n}} \times \mathcal{L}\mathbf{M}_S = 0 \qquad \text{(4b)}$$

for $\mathbf{r} \in S$. These expressions are referred to as the boundary condition equation.

A discrete version of the equations above is obtained by employing standard MoM techniques. Most authors employ RWG basis functions on flat triangular patches whereas a higher-order version using smooth polynomial basis functions on curved curvilinear patches were introduced in [14]. The data equation and the boundary condition equation leads to two coupled matrix equations

$$\bar{\mathbf{A}}\mathbf{x} = \mathbf{b}, \qquad (5)$$

$$\bar{\mathbf{L}}\mathbf{x} = \mathbf{0}, \qquad (6)$$

where $\mathbf{x}$ is a vector of unknown basis function coefficients, $\mathbf{b}$ contains samples of the measured field, $\bar{\mathbf{A}}$ is an $M \times N$ matrix with elements representing the field radiated by a particular basis function, and $\bar{\mathbf{L}}$ is a $P \times N$ matrix, whose elements represent the field radiated by a particular basis function, weighted by a particular testing function on the surface of reconstruction.

The coupled matrix equations above must be solved for the unknown current vector $\mathbf{x}$. However, the elements of $\mathbf{b}$ are inherently affected by measurement noise which may deteriorate the solution unless regularisation is employed. A common approach to this problem is to take advantage of the inherently regularising property of a Krylov-subspace solver and apply it to the equation

$$\begin{bmatrix}\bar{\mathbf{A}} \\ \bar{\mathbf{L}}\end{bmatrix}\mathbf{x} = \begin{bmatrix}\mathbf{b} \\ 0\end{bmatrix}. \qquad (7)$$

This solution method combined with a RWG discretization scheme has been used in the vast majority of previously published works, either in the simplest possible version with $\bar{\mathbf{L}} = 0$ in [3, 4, 5, 6, 8, 9, 10, 11], or more recently with a non-zero $\bar{\mathbf{L}}$ in [12, 13]. Smooth polynomial basis functions are required for improved accuracy but they at the same time need a more advanced solution scheme. The scheme introduced in [14] solves this problem by employing the matrix $\bar{\mathbf{L}}$ as a regularising term with a problem-dependent weight. In the present paper we employ an iterative variant of the advanced solution scheme in combination with higher-order basis functions. Results obtained with first-order basis functions and a simple iterative solution of (7) are presented for comparison.

3. NUMERICAL RESULTS FOR RMS ERROR AND ITERATION COUNT

The performance of the iterative variant of the higher-order method [14] has been investigated by considering analytical data with added noise. The use of analytical data allows the reconstructed currents to be compared to the exact solution and the relative RMS error can be computed. The test case is the same as "Case 1" in [14], i.e., 5 dipoles with arbitrary orientation inside a spherical reconstruction surface. The equivalent surface currents on the surface of reconstruction were obtained with two different algorithms:

1. First-order basis functions (roof-tops) in combination with a simple iterative solution of (7). The number of unknowns is $N = 2400$ and the number of patches is 600.
2. Higher-order basis in combination with an iterative variant of the solution scheme presented in [14]. The number of unknowns is $N = 864$ and the number of patches is 24.

For both algorithms the sphere is meshed using 4th-order curvilinear patches which provide an accurate geometrical model of the curved surface. The memory required to store the matrices $\bar{\mathbf{A}}$ and $\bar{\mathbf{L}}$ scales as $O(N^2)$ and the first-order algorithm therefore requires about ten times more memory than the higher-order version.

The relative RMS error versus the number of iterations performed by the Krylov subspace solver is shown in Figure 1. For noise-free data the first-order algorithm reaches an RMS error of about 20 percent after a few iterations but further improvements require a substantial number of iterations. The higher-order algorithm achieves a much lower RMS error and the error decays rapidly as the iteration count increases. This confirms the observation of [14]: Without noise the higher-order algorithm can reconstruct the field essentially without loss of information.

The results when noise is added are presented in the lower part of Figure 1. The first-order algorithm essentially provides the same accuracy as in the noise-less case whereas the higher-order algorithm diverges for large iteration counts. Therefore, it becomes crucial to stop the iterative algorithm when the optimal solution is obtained (see [14]). For the case considered here, the RMS error

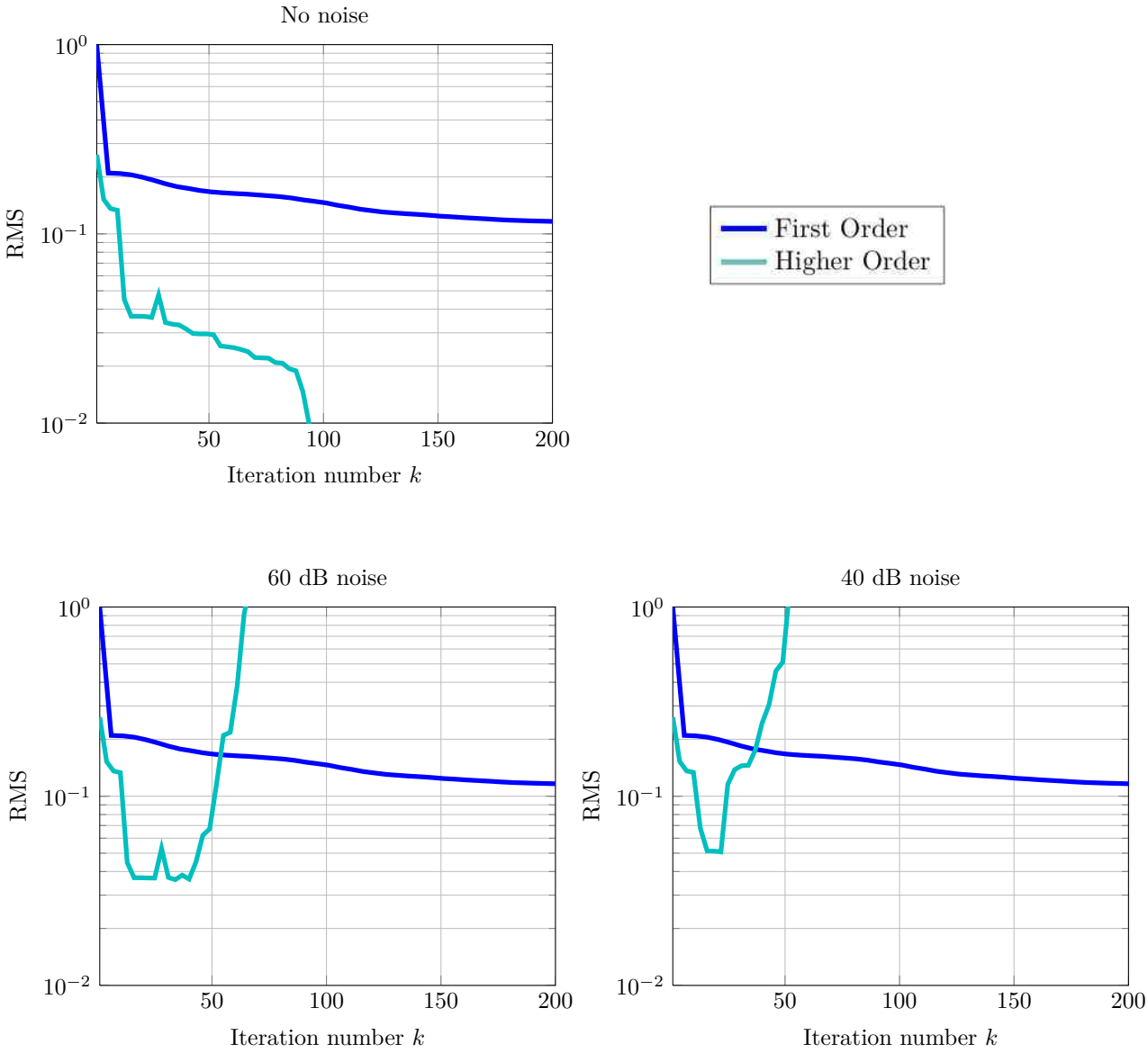

Figure 1. Relative RMS error versus iteration count. The higher-order method (light blue curve) corresponds to $N = 864$ polynomial basis functions. The first-order method (dark blue curve) corresponds to $N = 2400$ roof-top basis functions. Top left: Synthetic data with no added noise. Bottom left: Synthetic data with SNR=60 dB. Bottom right: Synthetic data with SNR=40 dB.

obtained with the higher-order algorithm is an order of magnitude lower than that obtained with the first-order version. In addition, it is noted that the higher-order algorithm uses an order of magnitude less memory.

4. APPLICATION EXAMPLES

The higher-order INV-MoM is now used to reconstruct the extreme near field for two practical cases: Three circular patch antenna elements in a large radiometer configuration and a corrugated horn antenna.

4.1. Radiometer antenna elements

The first test case considers three out of 69 circular patch antenna elements in the MIRAS instrument on ESA's SMOS satellite (see Figure 2). The radiation pattern of each antenna unit was measured at the DTU-ESA spherical near field test facility [15]. During this measurement campaign, two antenna units (BC03 and A01) were found to produce a higher cross-polar field than expected. Figure 3 shows the pattern of a correctly working unit (A01), a unit producing a 10 dB higher cross-polar component (BC03), and a unit producing a frequency-dependent cross-polar level (A05). These measured fields were used as input to the INV-MoM algorithm and the surface of reconstruction was chosen to be a small box enclosing the element. The reconstructed cross-polar field components on the top surface of the thermal insulation foil ($z = -5$ mm) are shown in Figure 4. The correctly working unit A01 (left column) produced a frequency-independent symmetric cross-polar field component with a relatively low amplitude. Unit BC03 (centre column) produced a much higher cross-polar level and only two lobes instead of four. Unit A05 (right column) produced a cross-polar field that increases slightly with frequency and becomes more asymmetric at the highest frequency. This shows that even small errors in the cross-polar fields can be detected by the higher-order INV-MoM.

4.2. Corrugated horn antenna

The corrugated horn antenna considered here is shown in Figure 5. The antenna is mounted on a metal frame which is covered by absorbers and the radiation pattern was measured in the DTU-ESA spherical near field test facility [15]. The radiation pattern at 10 GHz is shown in Figure 6 where an unexpected high on-axis cross-polar field component can be observed. The near field is then reconstructed on a circular cylinder as shown in Figure 7. The front face of the cylinder is located at the horn aperture at $z = 0$ and the radius of the cylinder corresponds to the actual horn radius (58.2 mm). The cross-polar field component radiated by the reconstructed currents is also evaluated in front of the aperture at $z = \lambda/4$ (see Figure 8) revealing a more clear picture of the reconstructed near

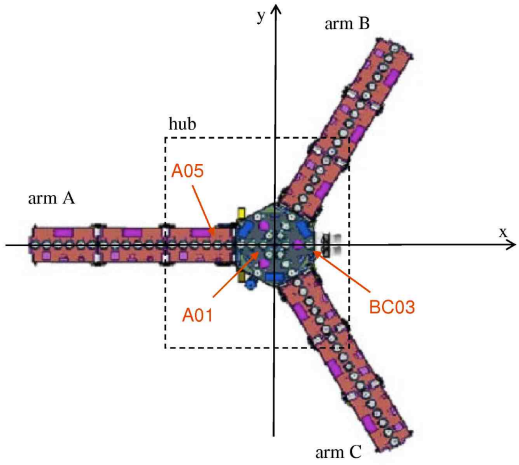

Figure 2. Configuration of the MIRAS instrument on ESA's SMOS satellite. The three antenna elements investigated here are marked with red arrows.

field. It is observed that the cross-polar field in front of the aperture looks distorted and lacks the expected symmetry.

The far field radiated by the reconstructed currents is also shown in Figure 6 along with the field obtained by truncating the measured SWE at the noise floor. At field levels below -40 dB, the field obtained by truncating the SWE looks like a low-pass filtered version of the noisy measured pattern. However, it is observed that the reconstructed far field does not agree with the truncated SWE field. The INV-MoM includes a priori information about the size and shape of the antenna, and one can therefore hope that the reconstructed pattern is more accurate than both the noisy measured pattern and the one obtained by truncating the SWE. It is obviously only possible to determine the most accurate pattern if the exact pattern is known and this was explored by using synthetic measured data. The radiation pattern of a corrugated horn, similar to the horn considered above, was evaluated by an accurate horn modeling tool and random noise was added in order to obtain a SWE with the same noise floor as the one obtained by the real measurements. The INV-MoM was then invoked with the noisy far field data as input. The surface of reconstruction was conformal to the geometrical model used in the horn modeling tool. Figure 9 shows the reference pattern obtained by the horn modeling tool, the noisy synthetic measurements, the reconstructed pattern obtained with INV-MoM, and the pattern obtained by truncating the SWE at the noise floor. The scale on the figure is relative to the co-pol peak at $\theta = 0$ and a random cut at $\phi = 46^\circ$ has been selected. It is seen that the reconstructed pattern (dashed blue curve) captures very fine details of the reference pattern (black circles) whereas the truncated SWE pattern is simply a low-pass filtered version of the noisy measured pattern. This result leads to the conclusion that the INV-MoM can be used to improve the measurement accuracy and reconstruct details of the measured pattern which are not

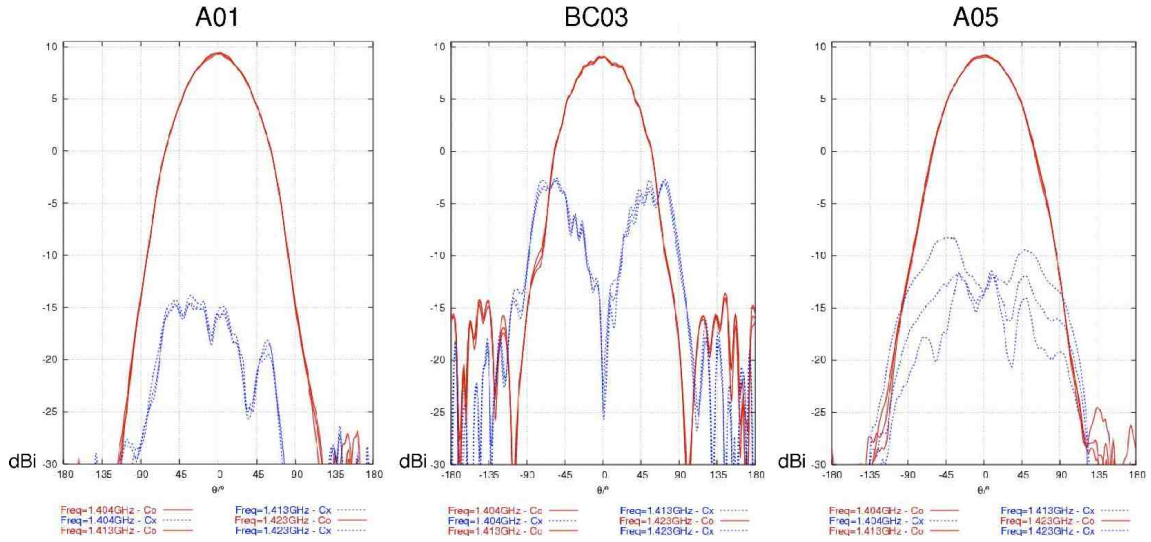

Figure 3. Radiation patterns of the three selected MIRAS antenna units. Each plot contains three frequencies. Unit A01 (left) is working correctly, unit BC03 (centre) produces a high cross-polar field component, and unit A05 (right) produces a slightly increased cross-polar field level that deteriorates with increasing frequency.

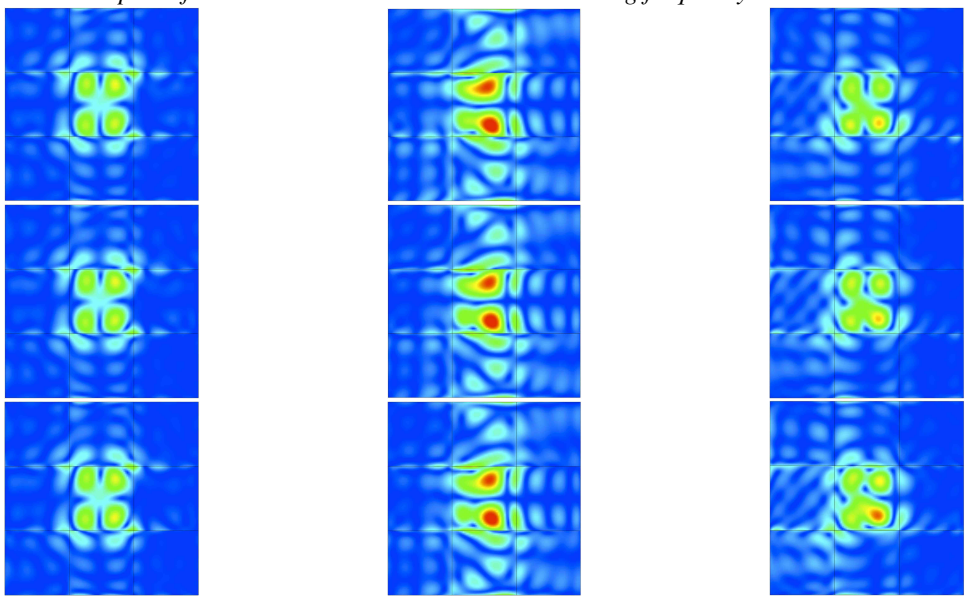

Figure 4. Reconstructed cross-polar field (E_y) at $z = -5$ mm. From top to bottom the rows correspond to 1.404 *GHz,* 1.413 *GHz, and* 1.423 *GHz. Left column: Correctly working unit A01. Centre column: Unit BC03 with high cross-polar field for all frequencies. Right column: Unit A05 with increasing cross-polar field levels for increasing frequency.*

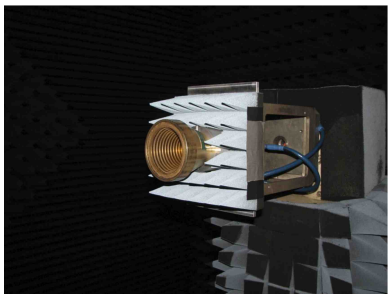

Figure 5. Measurement setup for the corrugated horn.

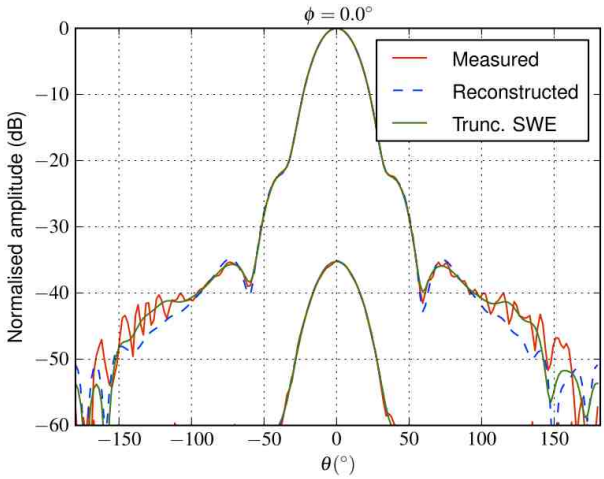

Figure 6. Measured (solid red curve) and reconstructed (dashed blue curve) radiation patterns of the corrugated horn. The pattern obtained by truncating the SWE at the noise floor (n=13) is also shown (solid green curve). The curve with a peak of -35 dB represents the cross-polar component.

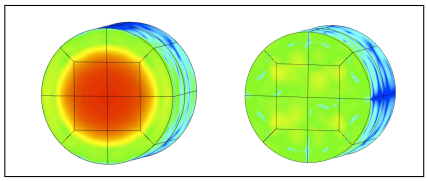

Figure 7. Reconstructed x- and y-components of the electric field in dB-scale shown directly on the surface of reconstruction.

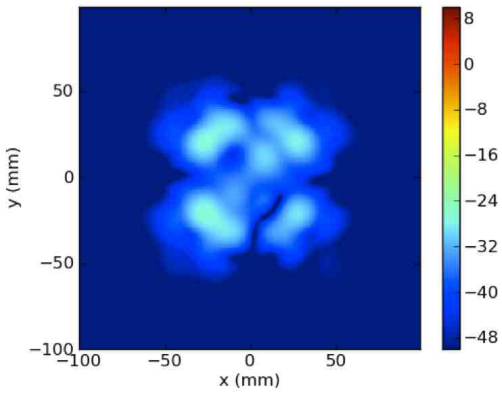

Figure 8. Cross-polar component of the reconstructed field at the $z = \lambda/4$ plane. The scale is normalised such that 0 dB corresponds to the level of the co-polar peak in the $z = \lambda/4$ plane.

directly available due to the inherent measurement noise. This is accomplished by utilizing the information about the location, size, and shape of the antenna. Figure 10 shows the spectrum of the SWE coefficients for the reference field, the synthetic measured field, and the reconstructed field. It is observed that the INV-MoM is able to recover a part of the spectrum that was not readily available due to noise.

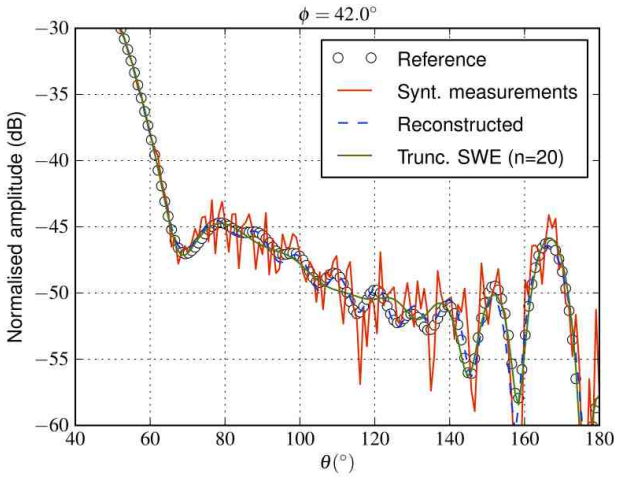

Figure 9. Reference pattern (black dots), the synthetically measured data with added noise (solid red curve), the reconstructed pattern (dashed blue curve), and the truncated SWE pattern (solid green curve).

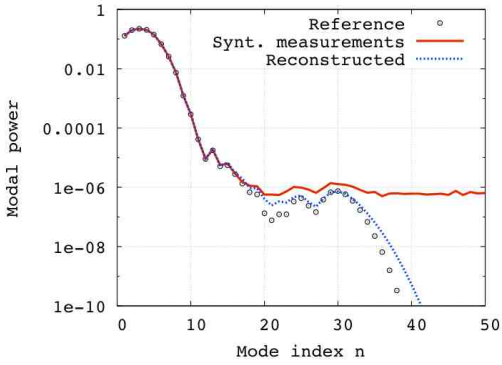

Figure 10. Power content of the SWE coefficients for the reference pattern (black dots), the synthetically measured data with added noise (solid red curve), and the reconstructed pattern (dashed blue curve).

5. CONCLUSIONS

This paper described an iterative variant of the higher-order Inverse Method of Moments technique for reconstruction of the extreme near field of an antenna. It was shown for analytical data with added noise that the accuracy of the higher-order algorithm is approximately an order of magnitude better than the first-order algorithm presented previously. The algorithm was applied to a practical antenna diagnostics problem where the reconstructed near field revealed anomalies of the antenna under test. Furthermore, an example was presented where the INV-MoM technique was used to enhance the measurement accuracy and reconstruct details of a measured pattern which were not directly available due to noise.

ACKNOWLEDGMENT

This work is supported by ESA/ESTEC within the ARTES 3/4 programme, ESTEC contract 22676/09/NL. The authors thank EADS CASA Espacio, Madrid, for permission to use the radiation pattern measurements of the MIRAS antenna units.

REFERENCES

1. Sarkar, T.K. & Taaghol, A. (1999). Near-field to near/far-field transformation for arbitrary near-field geometry utilizing and equivalent electric current and MoM, *IEEE Trans. Antennas Propagat.*, **47(3)**, pp. 566–573.

2. Persson, K. & Gustafsson, M. (2005). Reconstruction of equivalent currents using a near-field data transformation - with radome applications, *Progress in Electromagnetics Research*, **54**, pp. 179–198.

3. Las-Heras, F. & Sarkar, T.K. (2006). Evaluating near-field radiation patterns of commercial antennas, *IEEE Trans. Antennas Propagat.*, **54(8)**, pp. 2198–2207.

4. Alvarez, Y., Las-Heras, F. & Pino, M.R. (2007). Reconstruction of equivalent currents distribution over arbitrary three-dimensional surfaces based on integral equation algorithms, *IEEE Trans. Antennas Propagat.*, **55(12)**, pp. 3460–3468.

5. Alvarez, Y., T, K, S. & Las-Heras, F. (2007). Improvement of the sources reconstruction techniques: Analysis of the svd algorithm and the rwg basis functions, in *IEEE Antennas and Propagation Society International Symposium*, Honolulu, Hawaii, USA.

6. Alvarez, Y., Las-Heras, F., Pino, M.R. & Lopez, J.A. (2008). Acceleration of the sources reconstruction method via the fast multipole technique, in *IEEE Antennas and Propagation Society International Symposium*, San Diego, CA, USA.

7. Mioc, F., Quijano, J.A., Vecchi, G., Martini, E., Milani, F., Guidi, R., Foged, L.J. & Sabbadini, M. (2008). Source modelling and pattern enhancement for antenna farm analysis, in *30th ESA Antenna Workshop on Antennas for Earth Observation, Science, Telecommunication and Navigation Space Missions*, Noordwijk, The Netherlands, 555–559.

8. Eibert, T.F. & Schmidt, C.H. (2009). Multilevel fast multipole accelerated inverse equivalent current method employing rao-wilton-glisson discretization of electric and magnetic surface currents, *IEEE Trans. on Antennas Propag.*, **57(4)**, pp. 1178–1185.

9. Lopez, Y.A., Andres, F.L.H., Pino, M.R. & Sarkar, T.K. (2009). An improved super-resolution source reconstruction method, *IEEE Trans. Instrumentation and Measurement*, **58(11)**, pp. 3855–3866.

10. Schmidt, C.H., Ismatullah & Eibert, T.F. (2010). Comparison of lower and higher order basis functions in inverse equivalent current methods, *Applied Computational Electromagnetics Society (ACES) Conference, Tampere, Finland*.

11. Alvarez, Y., Las-Heras, F. & Pino, M.R. (2010). Antenna characterization using the sources reconstruction method, in *EuCAP Proceedings*, Barcelona, Spain.

12. Quijano, J.L.A. & Vecchi, G. (2009). Improved-accuracy source reconstruction on arbitrary 3-D surfaces, *IEEE Antennas and Wireless Propagation Letters*, **8**, pp. 1046–1049.

13. Quijano, J.L.A. & Vecchi, G. (2010). Field and source equivalence in source reconstruction on 3D surfaces, *Progress in Electromagnetics Research*, **PIER-103**, pp. 67–100.

14. Jørgensen, E., Meincke, P., Cappellin, C. & Sabbadini, M. (2010). Improved source reconstruction technique for antenna diagnostics,, in *Proceeedings of the 32nd ESA Antenna Workshop*, ESTEC, Noordwijk, The Netherlands.

15. Homepage of the DTU-ESA Facility. *http://www.elektro.dtu.dk/English/research/es/-afg/dtu_esa_facility/introduction.aspx*.